Light fragment spectra to upper kinematic limits for 300 MeV proton reactions with Be and Ag

R. E. L. Green,* R. G. Korteling, and J. M. D'Auria
Chemistry Department, Simon Fraser University, Burnaby, British Columbia, Canada V5A 1S6

K. P. Jackson and R. L. Helmer
TRIUMF, Vancouver, British Columbia, Canada V6T 2A3

(Received 5 August 1986)

Single particle inclusive spectra have been measured for the production of several isotopes of H, He, Li, and Be from the interaction of 300 MeV protons with Be and Ag targets. ^{1,2}H and ^{3,4}He fragments are measured over a wide range of energies which approach the upper kinematic limits at many of the angles measured. Measurements of the isotopically resolved He, Li, and Be fragments over a more limited energy range are also reported for 190 MeV protons incident on the same two targets. The spectra have been fitted with a phenomenological moving-source model used successfully in earlier studies. However, good fits were not obtained over the extended kinematic ranges measured in this study. A model-independent invariant cross section analysis applied to the ^{3,4}He data at 300 MeV is used to illuminate the problems that any statistical model will face in trying to explain fragment production at intermediate energies.

I. INTRODUCTION

This paper discusses the results[1] of experiments seeking to characterize the single particle inclusive spectra of fragments produced by the interactions of intermediate energy protons with complex nuclei. Previous work, with helium and heavier fragments emitted from silver targets, is reviewed and extended in Ref. 2. Work with light targets such as Be has not been as extensively reported, but is useful as an indication of target mass effects. Our previous work on Be(p,p′) and Be(p,d) inclusive spectra was done in association with (p,2p) and (p,pd) coincidence studies already reported.[3,4] When included with the additional Be target data reported here, a reasonably complete data set now exists for this representative light system. An extensive review of this general field has recently been published.[5]

The deficiency in the previous Ag target work which provided the main impetus for the work reported here was the lack of data at the higher fragment energies. For $Z \geq 3$, this was primarily due to the smallness of the cross sections involved and hence was not considered a compelling reason for extended work. However, previous He spectra terminated at significant cross sections because of energy limits in the equipment. Typically, only the lowest third of the possible energy range of these fragments was measured. At considerably lower incident proton energies, fragment spectra have been measured over essentially their entire kinematic range,[6] but the interesting region between the evaporative domain and the domain dominated by discrete final states is short at these lower incident energies. At 300 MeV incident energy, this intermediate region is the dominant feature of the spectra and it is possible to make interesting extensions of analyses, such as that done for the earlier truncated He spectra.[7] One section of this paper and an Appendix to it are devoted to such extensions.

While the main emphasis in this paper is on 300 MeV incident protons, we have made additional measurements at 190 MeV in order to provide more detailed information on incident energy dependences. The data have been fitted with the same phenomenological model applied to the 300 MeV data, but are otherwise reported without much additional comment since there do not appear to be any radical changes in the types of complex reactions initiated by protons of the two different energies.

II. EXPERIMENTAL TECHNIQUES

All measurements were performed in external proton beam lines at the TRIUMF accelerator. The inclusive spectra of high energy protons and deuterons were measured using the $T1$ target location in beam line 4B by methods previously detailed in a paper[3] where the ^{9}Be(p,p′) and ^{9}Be(p,2p) reactions at 300 MeV are discussed. In brief, these measurements were made with ΔE-E detector telescopes composed of plastic and NaI scintillators which were calibrated using pp scattering. Protons were identified on the basis of their ΔE and E signals and their cross sections were corrected for the NaI reaction tail events using a phenomenological fit to existing measurements. Deuterons which deposited their full energy in the NaI detectors were also easily identified. Their spectra were corrected for reaction tail events by assuming that the ratio of events in the reaction tails to events in the full energy deuteron peaks was identical to that for protons of equivalent range and then applying the same phenomenological fit used for the protons.

The remainder of the spectra reported here were measured in the 152 cm diam scattering chamber in the 4A beam line at TRIUMF using a telescope with two silicon surface barrier detectors followed by a high purity germanium (HPGe) detector. The targets used were typically 2 mg/cm^2. Beam currents ranged from 1 nA to 2 μA, de-

pending on the angles and isotopes being measured. Currents were monitored with a secondary emission monitor (SEM) located downstream of the target and, for most runs, also with a monitor telescope sensitive to helium fragments between selected energies (as used in earlier work[7,8]). Relative normalizations between angles are believed known to $\pm 10\%$ and absolute normalizations to $\pm 30\%$.

The principal solid state detector was mounted on a remotely rotatable arm in the scattering chamber. A 16 mm i.d. $\times 4$ mm thick copper collimator at 450 mm from the central axis was immediately followed by a 73.3 μm thick (300 mm^2) Si detector and then by a 1008 μm thick (450 mm^2) Si detector. These were mounted in front of a 0.05 mm stainless steel foil covered window in the cryostat housing the HPGe detector. As before,[8] the silicon detectors were calibrated with alpha sources and were used in a ΔE-E configuration to collect data on low energy fragments. Foldback of the energy spectra due to the dead layer caused by the cryostat's stainless steel window and by the HPGe lower level threshold prevented these Si ΔE-E measurements from extending completely to the Si range limits, thus yielding short gaps in our overall measured He spectra, but only at fragment energies previously studied. Figure 1 gives an example of the data obtained using the two Si detectors and previous analysis[8] techniques.

The HPGe detector is similar to detectors already described,[9] except that a guard ring has been included in the configuration by machining a circular groove into the Li contact surface. This leaves an active 27 mm diam by 15 mm thick central region surrounded by an active external guard ring. The detector was oriented so that particles entered through the thin contact surface. Using a combination of techniques from other systems,[10,11] a cryostat

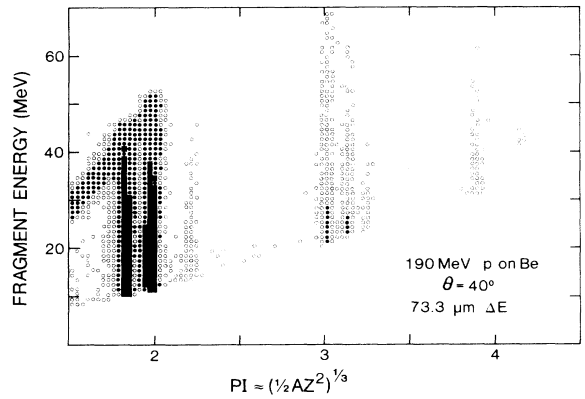

FIG. 1. A scatter plot of counts in the plane of particle identification value PI and total fragment energy for fragments measured at 40° from a 190 MeV proton beam incident on a Be target. The active detector elements for this plot consist of two Si surface barrier detectors; a significant number of the ^{3}He and ^{4}He fragments pass entirely through these elements and give rise to the diagonal band of incorrectly identified fragments and energies. Open circles indicate grid elements containing 1—3 counts; solid circles indicate 4—6 counts; solid squares indicate 7 or more counts. Recoil ^{9}Be nuclei from p-^{9}Be scattering are clearly seen.

for the detector was designed to fit in the 152 cm diam scattering chamber and operate independently of the state of its vacuum.

An initial energy calibration for the HPGe detector system was obtained by extrapolating from γ-ray source measurements. When the telescope was operational, deuteron spectra at 120° from 300 MeV protons incident on CH_2 and CD_2 targets were used to define relative fragment yields from the carbon. A subtraction of the proton spectra then yielded the protons from pd elastic scattering. Calibrations based on this energy were identical to the γ-ray calibrations within the $\pm 1\%$ accuracy of the measurements.

Primary identification of the energetic fragments in the solid state detector telescope relied on the energy ΔE_2 measured in the 1006 μm Si detector. This measured value was converted to an effective value

$$\Delta E_{\text{eff}} = \Delta E_2 \left[1.23 + 0.0376 \left[\frac{\Delta E_2}{E} \right]^{0.887} \right],$$

where E is the energy measured in the HPGe detector. This ΔE_{eff} corresponds to the energy loss in both Si detectors and in the stainless steel window; it is an empirical fit to the appropriate energy losses valid for all energies E above the HPGe threshold and for all fragment types discussed in this paper. This ΔE_{eff} was then used in the algorithm of Ref. 8 with the appropriate overall thickness for ΔE_{eff} in order to generate a particle identification value PI' for each HPGe event. A further minor slope correction

$$PI = PI' - 0.0003(E + \Delta E_{\text{eff}}),$$

where the energies are in MeV, was then applied. Over the nearly 300 MeV range of energies measured in the HPGe detector, this procedure yielded a unique range of PI values for each fragment type, independent of fragment energy. Secondary identification of He fragments using a similar procedure based on the 73.3 μm ΔE detector proved useful in reducing general background around the region of the He events, at the expense of slightly reduced efficiency for detecting valid events.

For most of the incident beam on target, the Si-HPGe detector telescope was run with a hardware cut in the electronics. It was generated using appropriately attenuated linear signals added in a summing amplifier as in Ref. 8. This allowed p and d fragments to be excluded from the data acquisition system without rejection of any He or heavier fragments. While this detector telescope was not optimized to measure hydrogen isotope fragments, these could be measured by reducing the beam current and removing this sum system hardware cut. Useful H isotope spectra are obtained where they are falling sufficiently rapidly with fragment energy that there is little contribution from higher initial energy fragments which pass through the copper collimator and into the active components of the telescope. The upper energy limit for H isotopes is less than the telescope range limit because there was no veto detector following the HPGe detector. The data are used only when the ΔE signals allow separation of particles which have gone completely through all detec-

tors from particles stopping in the telescope. Figure 2 gives examples of the data obtained with the Ge detector run both with and without the hardware cuts on hydrogen isotopes. It also indicates pileup of random coincidences as the rate limit in this experiment.

For protons which are just stopped by the HPGe detector, calculations[12,13] confirmed by measurements[9] near this region indicate that only 6% of these protons will deposit less than their full energies due to reactions while traversing the detector. On the basis of systematics indicated by calculations[14] and measurements[15–17] where proton-nucleus and nucleus-nucleus reaction cross sections can be compared, we expect reaction losses for He isotopes to be less than twice these proton values. We have therefore not made any corrections to our spectra for these losses since they are small and not well determined.

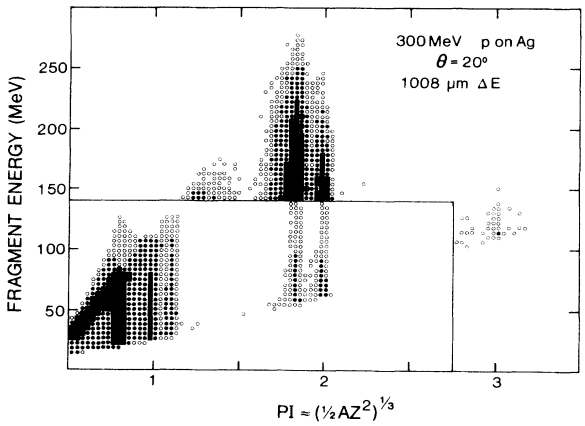

FIG. 2. A scatter plot of counts in the plane of *PI* value and total fragment energy for fragments measured at 20° from a 300 MeV proton beam incident on a Ag target. The active detector elements for this plot consist of a Si surface barrier detector and a 15 mm thick HPGe detector. The region outlined in the lower left corner shows data from a run with low beam current, while the remainder of the figure shows data from a run with high beam currents during which H isotopes were electronically rejected. A significant number of the p, d, and t fragments pass entirely through the HPGe detector and give rise to the diagonal band of incorrectly identified fragments. The counts in the region below the He isotopes in the high current data are due to signal pileup. High energy ^{6}Li fragments are visible above the background. Open circles indicate grid elements containing 2–4 counts; solid circles indicate 5–8 counts; solid squares indicate 9 or more counts.

III. RESULTS AND ANALYSIS

The results from this experiment are numerically tabulated and available through the Physics Auxiliary Publication Service.[1] Tabulations are given for every reaction at 190 and 300 MeV for which there is an entry in Table I. In the remainder of this section, these results are discussed in categories determined by the type of ejected fragment or by the type of analysis performed. Errors shown in the inclusive spectra data are statistical only and are smaller than the symbol when not indicated.

A. Fragments with $Z=1$

Figure 3 shows data for Ag(p,p')X at $E_p=300$ MeV. The low energy data at 120° and 160° were taken with the Ge detector system and the rest of the data were taken with the NaI scintillator system. The normalizations are independently determined for the two systems. Except for an overall scaling factor, the curves shown are merely smooth lines drawn through the previously reported Be(p,p')X data[3] at $E_p=300$ MeV. The overall scaling factor used is the atomic weight of Ag divided by that of Be; this provides a measure of the accuracy to which the proton inclusive cross section per target nucleon can be considered constant over a wide range of targets, as previously measured and discussed.[17–20,5] The claimed relationship is at least a reasonable approximation for these ^{1}H ejectiles, especially when one considers that the agree-

TABLE I. Slope parameters extracted using the fitting procedure of Ref. 2 for various (p,f) (f denotes fragment) reactions. Where values are enclosed in parentheses, the data extend into kinematic regimes where the model does not fit well. Numerical tabulations are available for all reactions with table entries.

	190 MeV		300 MeV		480 MeV[a]
	Be	Ag	Be	Ag	Ag
^{1}H			(25.7)	(27.8)	
^{2}H			(23.8)	(28.8)	
^{3}H			13.5	16.2	
^{3}He	8.7	13.1	(13.1)	(18.1)	23.9
^{4}He	6.5	9.1	(8.5)	(14.6)	14.4
^{6}He	4.8	8.9	5.3		
^{6}Li	5.7	8.7	6.7	11.0	14.9
^{7}Li	4.6	8.4	4.7	10.8	12.6
^{8}Li	4.3	7.8	b	9.5	12.5
^{7}Be	4.9	6.9	5.4	11.6	14.4
^{9}Be		5.5		9.5	9.6
^{10}Be		6.2		8.9	10.0

[a]Reference 2.

[b]Data are not sufficient to obtain a reasonable fit.

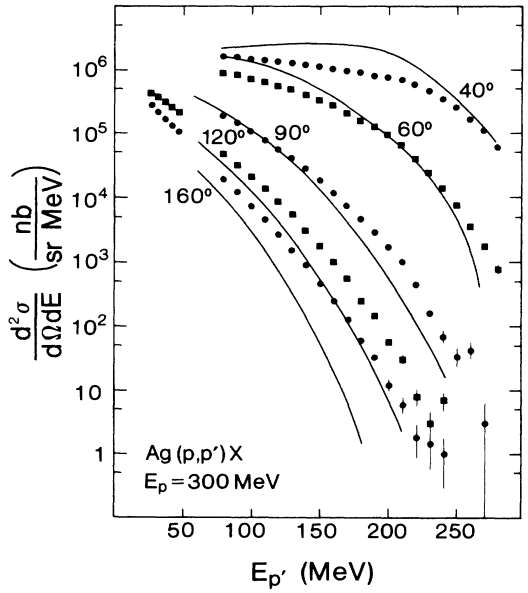

FIG. 3. Inclusive proton spectra at five angles for 300 MeV protons incident on Ag. The lines shown are smooth curves drawn through Be(p,p')X data (Ref. 3) at $E_p = 300$ MeV after multiplication by the ratio of the atomic weights of Ag and Be.

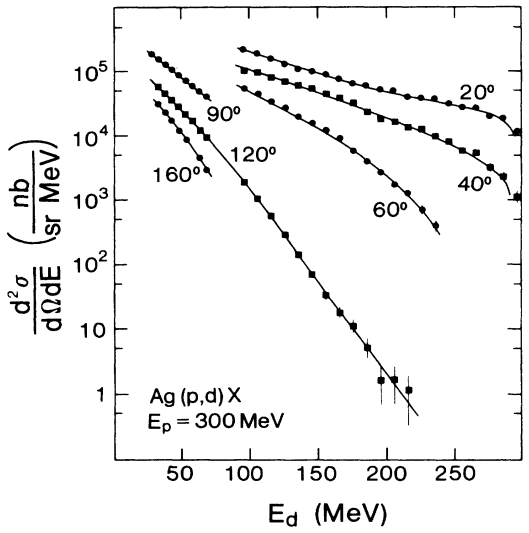

FIG. 4. Inclusive deuteron spectra at six angles for 300 MeV protons incident on Ag. Smooth curves have been drawn through the data.

ment will improve if comparisons are done using values from the center of mass systems for the two targets. (Both angles, which will no longer be fixed, and energies, will change. To lowest order, energy spectra for the transformed 90° spectra will change little, while the larger angle spectra for the Be target will increase relative to the Ag target spectra. At forward angles where the spectra are not monotonically decreasing with energy, the situation is more complicated.) The most notable difference appears to be a more pronounced quasielastic enhancement in the 40° and 60° spectra for the Be target, probably the result of a lower multiple scattering probability in the lighter target.

Figures 4 and 5 show deuteron inclusive spectra from 300 MeV protons incident on Ag and Be. Spectra at 90° and 160° could not be accurately extracted from the NaI detector system data, while forward angle spectra could not be accurately extracted from the Ge detector system data; these have been excluded from the figures. Smooth curves have been drawn through the silver target data. These curves have been scaled by the ratio of the Be atomic mass divided by the Ag atomic mass and transferred to the figure with the Be target data (the complement to the procedure used in Fig. 3). At higher angles, one again sees similar cross sections per target nucleon, but there is clearly an enhancement of high energy deuterons at 20° for the Be target. This may suggest considerable quasi-pd scattering, which may lend some support to models of backangle proton scattering which rely on related mechanisms.[21–25]

Figure 6 shows the large angle ^{3}H spectra from the Ag target at $E_p = 300$ MeV (only Ge detector system data are available), again compared to curves drawn through the Be target data and scaled to the same cross section per target nucleon. Hydrogen isotope spectra for $E_p = 190$ MeV have not been studied since a more extensive set of (p,n), (p,p'), and (p,d) measurements at this energy are in progress.[26]

B. Fragments with $A > 5$

Data collected for Li and Be fragments emitted from the Ag target extend the previous $E_p = 300$ MeV data set[8] to include three additional intermediate angles. As in the $E_p = 480$ MeV case, where a detailed extension[2] of the previous data was made, the main effect of the new information is to confirm the previous phenomenological description of the data and to allow this description to be

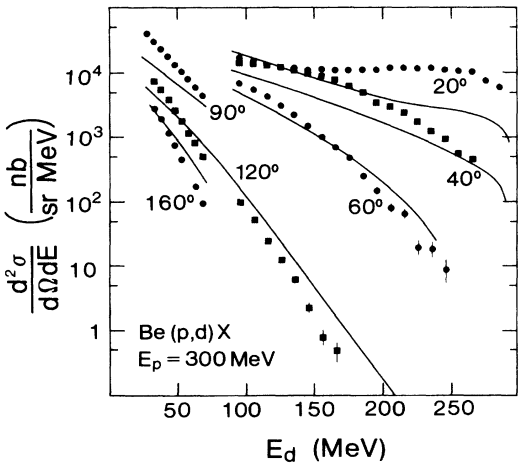

FIG. 5. Inclusive deuteron spectra at six angles for 300 MeV protons incident on Be. The smooth curves of Fig. 4 have been multiplied by the ratio of the atomic weights of Be and Ag and then transferred to this figure.

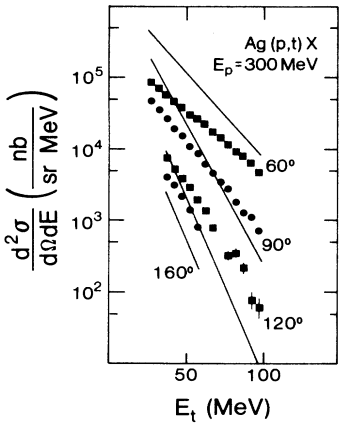

FIG. 6. Inclusive triton spectra at four angles for 300 MeV protons incident on Ag. Also shown are smooth curves drawn through the Be(p,t) data after multiplication by the ratio of the atomic weights of Ag and Be.

studied in greater detail. Similarly, the $E_p=190$ MeV data for the Ag target are basically an extension of the previous 210 MeV data.

In all cases, the Ag(p,f) data for $Z_f \geq 3$ can be described nicely by the combined evaporative and global nonevaporative fitting procedure of Ref. 2. The minor changes to the $E_p=480$ MeV parameters required to obtain the type of fits shown in Fig. 7 are quite appropriate for the changes in beam energy. However, while this model and the examples of its fits to the typical light fragment spectra shown in Figs. 7—9 serve as a convenient initial reference point, a detailed discussion of these is not given here. Such a discussion would be appropriate in this paper only if the model could be successfully applied over the more extended kinematic ranges of the He fragment spectra discussed later. We thus limit further discussion of the model to a few observations on the results of its application to the other data reported here.

The Li, Be, and ^{6}He fragments from the p + Be reactions are more accurately viewed as heavy residual nuclei than as light fragments. Figures 1 and 7—9 present some of the data obtained in this study. In Fig. 1, note the isolated peak from ^{9}Be elastic scattering. A detailed investigation of few body reactions in the p + ^{9}Be system via study of recoiling target residuals is the subject of a separate experimental program[27] and will not be pursued here. An attempt to apply the phenomenological model used in the Ag target case is shown in Figs. 7—9 for some of the continuum spectra from the Be target; no evaporation component has been included, as would seem appropriate for this light target. The fits obtained, even for fragments only two nucleons removed from the target as in Fig. 9, are of quality similar to those for the Ag target. This allows one to extract the model parameters, e.g., the slope parameters of Table I, although their interpretation may be difficult. As one would intuitively expect, the source velocities found for the Be target case are generally much larger than those for the Ag target. The correlation between fragment velocities and source velocities is also much stronger for the Be target. The parameters governing the position of the maxima and the widths of the spectra near the maxima are not well determined (nor important for fitting the regions containing data) for the Be target.

From Figs. 7 and 8, where identical fragments emitted from both Ag and Be targets may be compared, it can be seen that the cross sections per target nucleon are no longer comparable for these $A=6$ fragments.

C. ^{3}He and ^{4}He fragments

Figure 10 shows the ^{3}He and ^{4}He spectra from Ag for $E_p=300$ MeV. The exponential falloff in the 100—200

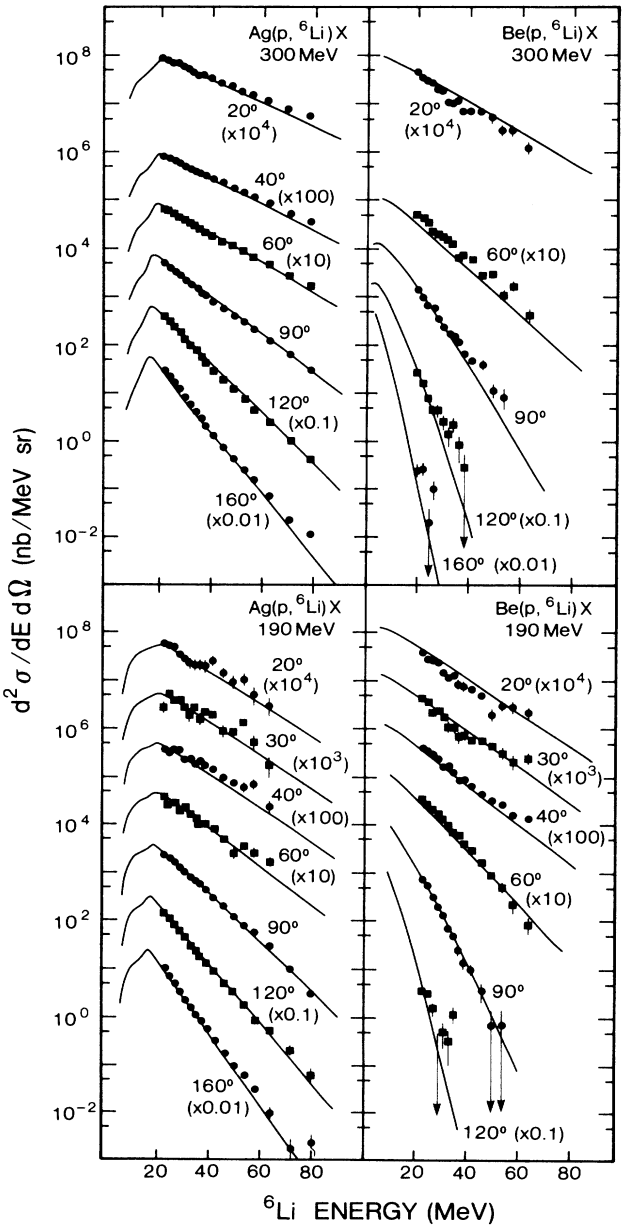

FIG. 7. Inclusive ^{6}Li spectra at various angles for 190 and 300 MeV protons incident on Be and Ag. The fits to the data were generated using the procedure of Ref. 2.

MeV range is approximately that expected from extrapolating previous measurements[7,28] in the lower fragment energy range. Above 200 MeV, the falloff appears to become progressively faster as the kinematic limit is approached. Within the statistics of the measurements, these spectra appear to change quite smoothly over the entire range above the maxima near an energy determined by the Coulomb barrier. The smallness of the cross sections prevents us from seeing structure associated with two-body final states.

The results of an attempt to fit the spectra using the procedure[2] applied to the heavier fragments in the preceding subsection is also shown in Fig. 10. The fits at lower fragment energies, where previous experience would suggest success, remain good even though the higher energy data points have been included in the data set to be fitted. The immediate causes of the failure of the fits to reproduce the higher energy data stem from at least two sources. First, the asymptotic form of the fragment energy dependence in the model assumes the fragment energy is significantly smaller than the kinematic limit; this leads to predictions which cannot follow the increasing rate of falloff at higher energies. Second, the form assumed for

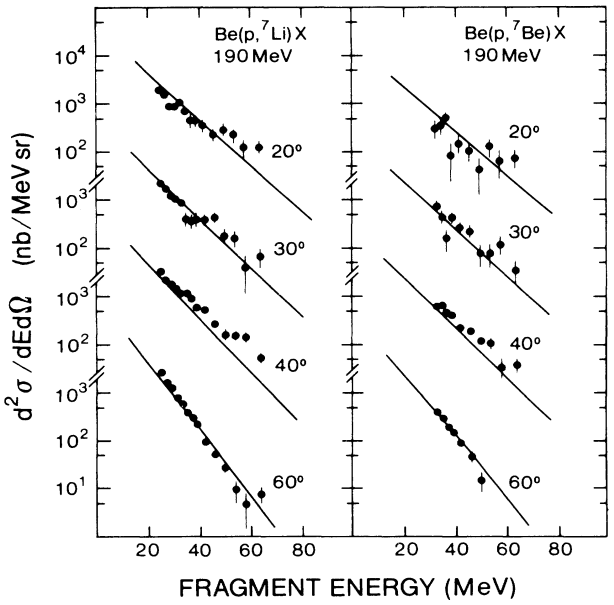

FIG. 9. Inclusive ^{7}Li and ^{7}Be spectra at various angles for 190 MeV protons incident on ^{9}Be. The fits to the data were generated using the procedure of Ref. 2.

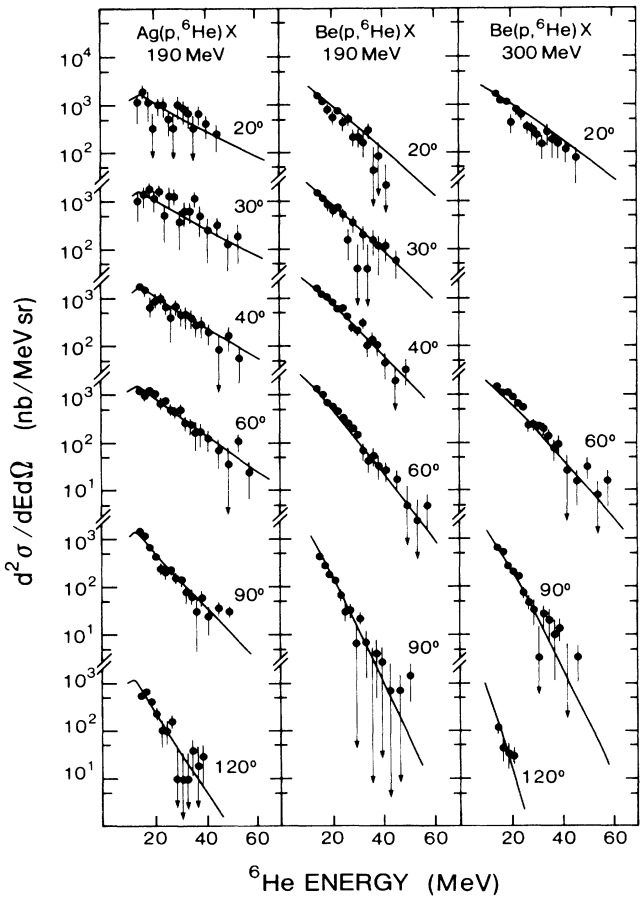

FIG. 8. Inclusive ^{6}He spectra at various angles for 190 MeV protons incident on Be and Ag and for 300 MeV protons incident on Be. The fits to the data were generated using the procedure of Ref. 2.

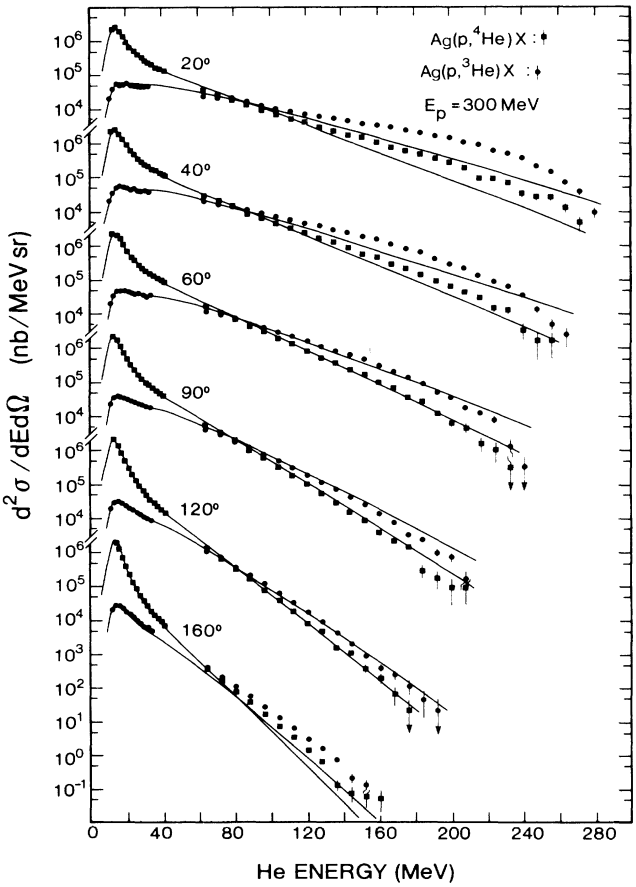

FIG. 10. Inclusive ^{3}He and ^{4}He spectra at six angles for 300 MeV protons incident on Ag. The curves shown are the result of attempting to fit the data using the procedure of Ref. 2.

the correlation between fragment velocity and source velocity is not constrained to be asymptotically correct; this will effect the way the angular dependence of the spectra is fitted, but not necessarily in a simple way due to coupling with other parameters. The overall fit balances these obvious deficiences to minimize deviations, although not very successfully. Modifications to correct the above deficiencies are possible, but it is not clear that the added complications would be fruitful in light of the analysis to be discussed in the next subsection. It is quite possible that the underlying assumptions in the fitting procedure are not applicable in this fragment energy regime.

Figure 11 shows the ^{3}He and ^{4}He spectra from Be for $E_p = 300$ MeV. Two experimental features deserve comment. First, in both the ^{3}He and ^{4}He spectra at 20°, there appears to be significant enhancement of the cross section in regions centered about the He energies corresponding to elastic p-He scattering, even to the point of a statistically significant increase in ^{3}He cross section with increasing energy just above 160 MeV. Second, the low energy regions of the ^{4}He spectra show a distinct change in slope over a relatively short span in energy, perhaps due to an additional reaction mechanism with high yields at low energies (reminiscent of the evaporation component in Ag target data).

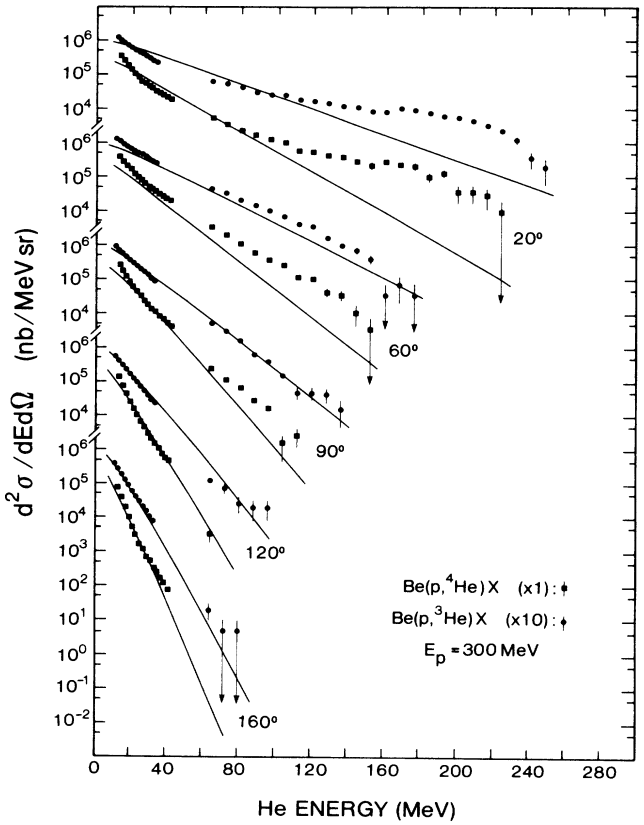

FIG. 11. Inclusive ^{3}He and ^{4}He spectra at five angles for 300 MeV protons incident on Be. The curves shown are the result of attempting to fit the data using the procedure of Ref. 2. Note that the data and the curves for the ^{3}He fragments have been multiplied by 10 before plotting. The recoil energies of ^{3}He and ^{4}He from free p-He elastic scattering are, respectively, 205 and 178 MeV at 20°.

The results of applying the fitting procedure of Ref. 2 are also shown in Fig. 11. Since no evaporation component has been assumed in the Be target case, there is no hope of fitting the change in slope at low ^{4}He energies. There is also nothing in the model which yields enhancements in the quasielastic scattering regions. Hence, at least at forward angles, the fits are not good.

The failure of the fitting procedure for He isotopes over extended kinematic regions does not preclude overlooking the failures by attributing them to reaction mechanisms not accounted for by the model and then assuming the remaining cross section is accounted for by the model. A similar philosophy has previously been applied to proton inclusive spectra, where there are known to be significant direct components.[20] In this case, reasonable moving source fits were obtained for a number of different cases when the data excluding the quasielastic region were used. In applying our fitting procedure to the inclusive (p,p′) and (p,d) data reported here, fits of comparable quality to those in Fig. 11 were obtained. [Good fits to the (p,t) data were obtained due to its limited range.] We report the results for the temperature-like parameter of these fits in Table I because of the apparent interest in this quantity;[5] it should be used with caution.

Figure 12 shows the inclusive ^{3}He and ^{4}He spectra for both Ag and Be targets at $E_p = 190$ MeV. Data are limited to the lower fragment energies and consequently reasonable fits are obtained using the model of Ref. 2 for all cases except Be(p,^{4}He). For Be(p,^{4}He), the same change in slope seen at 300 MeV again appears and cannot be fitted without adding a second type of reaction mechanism. It also appears that the 60° data from this case are unusually high, although it is hard to separate normalization uncertainty and model dependence from this judgement.

The comparison of He cross sections per target nucleon are most easily done with Figs. 13–16 discussed in the next subsection since kinematic effects can be accounted for more easily using them. Obviously there must be some differences, e.g., the Ag target data show no strong quasielastic enhancement. However, if one does some fairly vigorous smoothing of the cross section (as, for example, by using the fits shown in Figs. 13–16) and compares the ^{4}He contours for an appropriately selected relative velocity between the two systems, the cross sections per target nucleon are in approximate agreement above the 10^{-2} nb/[(MeV/c)(MeV sr) (target nucleon)] level. (The optimum relative velocity is between that for comparisons in the laboratory frames and that for comparisons in the center of mass frames.) For the ^{3}He contours, a relative velocity can be found for the two systems such that values around 10^{-1} nb/[(MeV/c)(MeV sr) (target nucleon)] are nearly coincident, but other regions do not agree well. If more detailed comparisons are sought in the future, it appears that it would be useful to adjust incident projectile energies to yield total compound systems with identical energies available to the fragments being compared, i.e., incident energies such that the fragment

kinematic limits would be identical if the centers of mass were overlaid. Otherwise, purely kinematic effects will prevent comparisons at higher fragment energies, as is the case here.

D. Implications for statistical models from He fragment invariant cross sections

Figures 13—16 show sets of data points of constant invariant cross section $(1/p)(d^2\sigma/d\Omega\, dE)$ in the $(p_{||}/mc, p_\perp/mc)$ plane, where $p_{||}$ and $p_\perp$ are the parallel and perpendicular components of the fragment momentum p, and m is the fragment mass. The variable $p_{||}/mc$ rather than the rapidity y is used for simplicity in graphics; for the analysis used here this will give equivalent results to previous analyses using rapidities, since the source frame velocities considered will all be nonrelativistic [the relativistic character of emitted fragments merely shifts the apparent source position to values of $p_{||}/mc$ equal to the source velocity β_s times the factor $\gamma=(mc^2+E')/mc^2$, where E' is the fragment kinetic energy in the frame with velocity β_s]. To find values of fragment momentum corresponding to a given invariant cross section, an interpolation between the nearest two

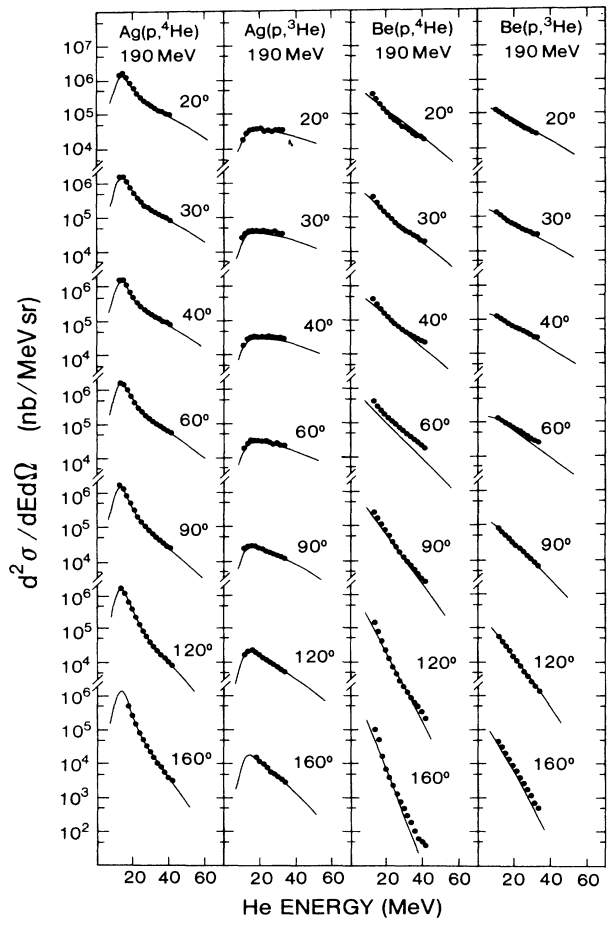

FIG. 12. Inclusive ^{3}He and ^{4}He spectra at seven angles for 190 MeV protons incident on Be and Ag. The fits to the data were generated using the procedure of Ref. 2.

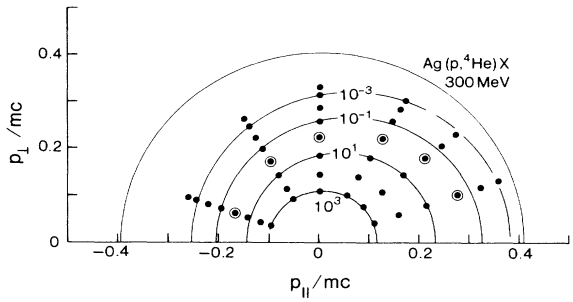

FIG. 13. Sets of data points with invariant cross sections equal to 10^n nb/[(MeV/c)(MeV sr)] for integer values of n decreasing with radial distance from the origin. The $n=0$ data points are circled. The outermost circular line is the kinematic limit for the reaction. Inner circular lines are attempts to fit isotropic emission from sources moving in the beam direction to data with the indicated values. The reaction is Ag(p,^{4}He) at 300 MeV.

data points was made assuming an exponential dependence of the invariant cross section on fragment momentum. Statistical errors were also interpolated under these assumptions for use in fitting procedures. (A recent study of the average momentum transferred to heavy targets by a series of projectiles has been reported by Fatyga *et al.*[29]).

The outermost curves in Figs. 13—16 are the kinematic limits for the emitted fragment. The data points indicated are at values of 10^n nb/[MeV sr)(MeV/c)] for integer values of n decreasing with distance from the origin along each set of points on a given radial line. The value of 10^0 is indicated by an extra ring around the data point. The remaining curves are fits (independently done for each contour level shown) for isotropic emission from a single moving source; the fit is chosen to yield the minimum value of χ^2 for the labeled value of invariant cross section, using the statistical errors only for the data. (χ^2 decreases and there are minor changes in the parameters if estimates for errors in relative normalizations between angles are added.) The curves are dashed where the statistical accuracy of the data limited measured cross sections to values higher than the labeled curve.

For the Ag target, the region near the origin has already been analyzed in a similar fashion,[7] including both the low energy and high energy sides of the maximum in

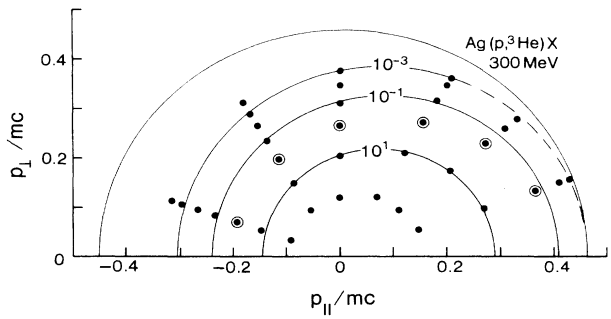

FIG. 14. Same as Fig. 13, except the reaction is Ag(p,^{3}He) at 300 MeV.

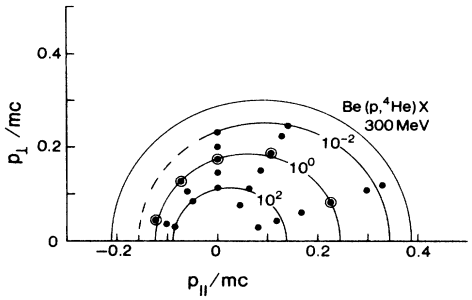

FIG. 15. Same as Fig. 13, except the reaction is Be(p,^{4}He) at 300 MeV.

the ^{4}He spectrum. The beginnings seen there of deviations from such single source fits are quite prominent in some regions of the more kinematically complete data set presented here. In some cases shown in Figs. 13—16, the fits and data differ by more than an order of magnitude. However, the largest deviations in fragment radial velocities occur in the midrange values, where differences in cross section are not as dramatic.

If one accepts at face value the two parameters, source velocity β_s and fragment radial velocity β_r, from each of the fits in Figs. 13—16, one can see that β_s appears to reach a limit ($\lesssim 0.1$) long before β_r approaches the kinematic limit. If such fits were valid as one approached the kinematic limits, β_s would, of course, eventually retreat to the center of mass velocity as the cross section became sufficiently small and β_r correspondingly approached the kinematic limits at all angles. One immediate implication of these results is that the relationship between β_r and β_s assumed in the fitting procedure of Ref. 2 does not apply at these higher fragment energies. A more significant implication for extending this model arises, however, from the fact that β_s and β_r can no longer be uniquely related, i.e., no change in the functional relationship between β_s and β_r in the model will ever be sufficient to achieve fits to this data.

This last conclusion does not yet mean we have eliminated statistical mechanism as possible explanations of this data. (In this paper, we are using the term statistical mechanisms in the very general sense that, for the observed product, the last step in its production is emission from any of a number of subsystems in a manner consistent with an experimental definition of statistical process—namely symmetric emission in the moving frame of any particular subsystem, specialized in most of the work here to isotropic emission in this frame.) The Appendix is a generalized consideration of purely isotropic emission from each of an ensemble of sources where the nature of a source is allowed to be a function of its velocity (as, for example, a higher temperature for cases with higher source velocities). The crucial question is whether integration over such an ensemble of sources can reproduce the measured data. The answer for a physically meaningful ensemble is by no means clear, although it is possible to investigate further the feasibility that such a fit is possible. This is done in the Appendix for an unpolarized incident beam by considering the Taylor series expansion of the integral over an ensemble of moving isotropic sources under the assumption that the source velocities are not highly relativistic. For a fixed fragment energy E, all terms containing powers of source velocity squared or lower can be collected to write the invariant cross section as

$$F(E,\theta)=A_0(E)+A_1(E)\cos\theta+A_2(E)\cos^2\theta+\cdots ,$$

where any additional angular dependence can arise only from terms involving higher powers of the source velocity.

In most past analyses, we have been able to find, for any given E, a reference frame in which $A_n(E)=0$ for $n\neq 0$. There are no such reference frames for most of the data in Figs. 13—16. To investigate the feasibility of fitting these data by including higher order terms in source velocity, χ^2 per degree of freedom for the fits yielding the contour levels shown in the figures (using only A_0 terms) were compared to those for the same values of β_r when A_1 and A_2 terms were also allowed. For the Be target, these reduced χ^2 values increased for four of the five contour levels where the extended fit was possible. The value for the fifth contour was marginally lower. For the Ag target, the extended fits gave lower reduced χ^2 values in all cases, sometimes dramatically. This suggests that pursuit of statistical mechanisms as an explanation of the data may be fruitful for the heavier target, but is unlikely to be so for the lighter target.

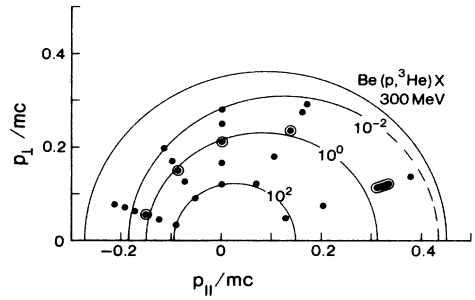

FIG. 16. Same as Fig. 13, except the reaction is Be(p,^{3}He) at 300 MeV. The elongated data point at 20° for the 1 nb/[(MeV/c)(MeV sr)] level represents the fact that the data actually pass through this level three times in this region due to the structure which can be seen in the data in Fig. 11.

IV. SUMMARY AND CONCLUSIONS

When single particle inclusive energy spectra resulting from medium energy reactions are examined over their entire kinematic regime, it is clear that the vast majority of the cross section for most ejectiles is the result of complex reactions. Cross sections from identifiable single-process direct reactions plus those from statistical decay of fully equilibrated residual nuclei rarely account for even half of the total cross section for most ejectile species. Whether the relatively smooth variation of these spectra with kinematic variables can be described by some model which appropriately averages over the many complex reactions is not yet obvious. A phenomenological description has been developed which appears to work

well at lower energies of emitted fragments, but the data presented here show that its extension to higher fragment energies at the least requires modification and at the worst may not be possible. No model yet put forward seems capable of tracking the behavior of single particle inclusive spectra over their entire kinematic domains. For several ejectiles, the data presented in this paper and its associated tabulation[1] map out a sufficient fraction of this domain that a reasonable test of any proposed wide-range model can be made. The preliminary analysis presented here may aid in guiding the search for more fully encompassing descriptions of such data.

In particular, there is no means by which a statistical model relying on a source with a fixed velocity can reproduce the data. Statistical models with multiple source velocities may still be capable of fitting the data, although even this seems unlikely for the Be target since the fit to this data worsens when a more detailed expansion for a generalized statistical model is considered. It seems likely the Be data can best be fitted by considering a series of direct interactions followed by final state interactions. For the Ag target, the fitting procedure of Ref. 2 appears capable of fitting the majority of the fragment cross sections, but not necessarily over the majority of the kinematic domain. For this target, we have not been able to rule out the possibility that a suitable modification of the model might fit over a much extended kinematic regime. If such an extension were found, it would perhaps only mean that the increased size of the target allows a larger number of final state interactions to wash out initial structure than in lighter targets and that no true statistical source was formed.

ACKNOWLEDGMENTS

The authors wish to thank R. H. Pehl for his assistance and guidance during the purchase and assembly of the HPGe detector systems used in this study. Useful information on cryostat design from R. A. Ristinen and D. L. Friesel was also much appreciated, as was the careful implementation of the design by the Simon Fraser University Science Machine Shop. We greatly appreciate the work of N. Bohna in processing the data through the Simon Fraser University Computing Center and in compiling and checking the data tabulations associated with this paper. We acknowledge with thanks the help received from the operations staff of TRIUMF in obtaining the proton beams used in this experiment. This work was supported by the Natural Sciences and Engineering Research Council of Canada.

APPENDIX

The invariant cross section F for inclusive production of a given fragment with momentum-energy 4-vector components $(p_x,p_y,p_z,iW/c)$ and rest mass m in a given reference frame can be formally decomposed as

$$F(p_x,p_y,p_z)=\int\int\int ds_x ds_y ds_z \times f(s_x,s_y,s_z;p_x',p_y',p_z') , \quad \text{(A1)}$$

with

$$\begin{bmatrix} p_x' \\ p_y' \\ p_z' \\ iW'/c \end{bmatrix} = c_{\mu\nu}(s_x,s_y,s_z) \begin{bmatrix} p_x \\ p_y \\ p_z \\ iW/c \end{bmatrix} , \quad \text{(A2)}$$

where $c_{\mu\nu}$ is the Lorentz transformation matrix. It can be interpreted as arising from a distribution of sources which, in their own rest frames, decay to yield invariant cross sections of $f(s_x,s_y,s_z;p_x',p_y',p_z')$.

We now define a pure hot spot model where post-emission modifications are not invoked by f isotropic in its own moving frame, i.e.,

$$f(s_x,s_y,s_z;p_x',p_y',p_z')=f(s_x,s_y,s_z;W' =f(s_x,s_y,s_z;|\mathbf{p}'|) , \quad \text{(A3)}$$

identical for any combination of p_x', p_y', and p_z' yielding a given

$$W'=c(m^2c^2+|\mathbf{p}'|^2)^{1/2} =c[m^2c^2+(p_x')^2+(p_y')^2+(p_z')^2]^{1/2} .$$

While Eq. (A1) with f of this form has the formal solution

$$f(s_x,s_y,s_z;W')=F(p_x,p_y,p_z)\delta(W'-mc^2) ,$$

we are concerned here with the more physically interesting case where $f(s_x,s_y,s_z;W')$ is assumed to be extensive in W' (and presumably not so extensive in s_x, s_y, and s_z). The question of whether there exist f of the form in Eq. (A3) is thus addressed in this Appendix for a selected subset of the possible systems.

Let us assume we have chosen our fragment momenta such that $|\mathbf{p}'-\mathbf{p}|/|\mathbf{p}| \ll 1$ for all $(s_x,s_y,s_z)=\mathbf{s}$ of interest and that we can make a meaningful Taylor series expansion of f in the $\mathbf{p}'$ variables about $\mathbf{p}$. Defining $\mathbf{h}=\mathbf{p}'-\mathbf{p}'$ and

$$\nabla=\frac{\mathbf{i}\partial}{\partial p_x'}+\frac{\mathbf{j}\partial}{\partial p_y'}+\frac{\mathbf{k}\partial}{\partial p_z'} ,$$

Eq. (A1) can then be written

$$F(\mathbf{p})=\int\int\int d\mathbf{s}[f(\mathbf{s},\mathbf{p})+(\mathbf{h}\cdot\nabla)f(\mathbf{s},\mathbf{p}) +\tfrac{1}{2}(\mathbf{h}\cdot\nabla)^2 f(\mathbf{s},\mathbf{p})+\cdots] , \quad \text{(A4)}$$

which for f isotropic as in Eq. (A3) becomes (with $h=|\mathbf{h}|$, $p=|\mathbf{p}|$, etc.)

$$F(\mathbf{p})=\int\int\int d\mathbf{s}\{f(\mathbf{s},p)+(\mathbf{h}\cdot\mathbf{p}/p)[df(\mathbf{s},p)/dp'] +(p^{-3}/2)[h^2p^2-(\mathbf{h}\cdot\mathbf{p})^2][df(\mathbf{s},p)/dp']+(p^{-2}/2)[(\mathbf{h}\cdot\mathbf{p})^2][d^2f(\mathbf{s},p)/dp'^2]+O(h^3)\} , \quad \text{(A5)}$$

where all terms of order h^2 or lower are given explicitly as indicated by the notation $O(h^3)$. Now use the Lorentz transformation to write

$$\mathbf{h}=\mathbf{p}'-\mathbf{p}=[(\mathbf{s}\cdot\mathbf{p}/s^2)(\gamma-1)-(\gamma W/c^2)]\mathbf{s} ,$$

where $\gamma=(1-s^2/c^2)^{-1/2}$ and thus write

$$F(\mathbf{p})=\int\int\int d\mathbf{s}\{f(\mathbf{s},p)+(p^{-1}c^{-2})[\tfrac{1}{2}(\mathbf{s}\cdot\mathbf{p})^2-W(\mathbf{s}\cdot\mathbf{p})][df(\mathbf{s},p)/dp']$$
$$+(p^{-3}c^{-4}/2)[W^2s^2p^2-W^2(\mathbf{s}\cdot\mathbf{p})^2][df(\mathbf{s},p)/dp']$$
$$+(p^{-2}c^{-4}/2)[W^2(\mathbf{s}\cdot\mathbf{p})^2][d^2f(\mathbf{s},p)/dp'^2]+O(s^3)\} , \quad \text{(A6)}$$

where all terms through order s^2 are given explicitly.

If the s dependence is now taken to describe a distribution of sources and we consider an unpolarized beam, we can orient a spherical polar coordinate system along the beam direction and write

$$f(\mathbf{s};p)=f(s,\theta_s;p) ,$$

where the symmetry of the situation eliminates dependence on ϕ_s. If we now consider $\mathbf{p}=(p,\theta,\phi)$ in this same coordinate system, we can write

$$\mathbf{p}\cdot\mathbf{s}=ps(\sin\theta\cos\phi\sin\theta_s\cos\phi_s$$
$$+\sin\theta\sin\phi\sin\theta_s\sin\phi_s+\cos\theta\cos\theta_s)$$

and use the integrals over ϕ_s to eliminate many of the resulting terms. Pulling the angular dependence of $\mathbf{p}$ outside the integrals (and using $\sin^2\theta+\cos^2\theta=1$) results in

$$F(p,\theta)=A_0(p)+A_1(p)\cos\theta+A_2(p)\cos^2\theta$$
$$+\int\int\int d\mathbf{s}\,O(s^3) , \quad \text{(A7)}$$

where the A_n are the results of integrals which could, in principle, be evaluated if $f(s,\theta_s;p)$ was known. This is the result used in the text.

*Present address: Los Alamos National Laboratory, Los Alamos, NM 87545.

[1]See AIP document PRVCA-35-1341-42 for 42 pages of numerically tabulated histograms of the single particle inclusive spectra discussed in this article. Order by PAPS number and journal reference from American Institute of Physics, Physics Auxiliary Publication Service, 335 East 45th St., New York, NY 10017. The price is $15 for microfiche, or $6.80 for photocopies. Airmail additional. Make check payable to American Institute of Physics.

[2]R. E. L. Green, R. G. Korteling, and K. P. Jackson, Phys. Rev. C **29**, 1806 (1984).

[3]R. E. L. Green, D. H. Boal, R. L. Helmer, K. P. Jackson, and R. G. Korteling, Nucl. Phys. **A405**, 463 (1983).

[4]R. L. Helmer, R. E. L. Green, K. P. Jackson, and R. G. Korteling, Phys. Rev. C **29**, 676 (1984).

[5]D. H. Boal, in *Advances in Nuclear Physics*, edited by J. W. Negele and E. Vogt (Plenum, New York, 1985), Vol. 15, pp. 85–214.

[6]J. R. Wu, C. C. Chang, and H. D. Holmgren, Phys. Rev. C **19**, 698 (1979).

[7]R. E. L. Green and R. G. Korteling, Phys. Rev. C **18**, 311 (1978).

[8]R. E. L. Green and R. G. Korteling, Phys. Rev. C **22**, 1594 (1980).

[9]J. F. Amann, P. D. Barnes, S. A. Dytman, J. A. Penkrot, A. C. Thompson, and R. H. Pehl, Nucl. Instrum. Methods **126**, 193 (1975).

[10]R. A. Ristinen, private communication. See also University of Colorado Nuclear Physics Laboratory Technical Progress Report NPL-816, 1978, pp. 163–166.

[11]D. L. Friesel, private communication. See also Indiana University Cyclotron Facility Technical and Scientific Report, 1978, pp. 153–157.

[12]D. F. Measday and C. Richard-Serre, Nucl. Instrum. Methods **76**, 45 (1969).

[13]M. Q. Makino, C. N. Waddell, and R. M. Eisberg, Nucl. Instrum. Methods **60**, 109 (1968).

[14]R. M. De Vries and J. C. Peng, Phys. Rev. C **22**, 1055 (1980).

[15]J. R. Wu, C. C. Chang, and H. D. Holmgren, Phys. Rev. C **19**, 370 (1979).

[16]J. R. Wu, C. C. Chang, and H. D. Holmgren, Phys. Rev. C **19**, 659 (1979).

[17]S. Frankel, W. Frati, G. Blanpied, G. W. Hoffmann, T. Kozlowski, C. Morris, H. A. Thiessen, O. Van Dyck, R. Ridge, and C. Whitten, Phys. Rev. C **18**, 1375 (1978).

[18]G. Roy, L. G. Greeniaus, G. A. Moss, D. A. Hutcheon, R. Liljestrand, R. M. Woloshyn, D. H. Boal, A. W. Stetz, K. Aniol, A. Willis, N. Willis, and R. McCamis, Phys. Rev. C **23**, 1671 (1981).

[19]D. H. Boal in Proceedings of the Relativistic Heavy Ion Winter School (Banff, 1982) (unpublished), available as TRIUMF Report TRI-PP-82-7.

[20]D. H. Boal and J. H. Reid, Phys. Rev. C **29**, 973 (1984).

[21]T. Fujita and J. Hüfner, Nucl. Phys. **A314**, 317 (1979).

[22]T. Fujita, Phys. Rev. Lett. **39**, 174 (1977).

[23]T. Fujita, Nucl. Phys. **A324**, 409 (1979).

[24]V. I. Komarov, G. E. Kosarev, H. Müller, D. Netzband, T. Stiehler, and S. Tesch, Phys. Lett. **80B**, 30 (1978).

[25]V. I. Komarov, G. E. Kosarev, H. Müller, D. Netzband, V. D. Toneev, T. Stiehler, S. Tesch, K. K. Gudima, and S. G. Mashnik, Nucl. Phys. **A326**, 297 (1979).

[26]J. M. D'Auria, private communication.

[27]K. P. Jackson, G. Bichoff, D. H. Beal, J. M. D'Auria, R. E. L.

Green, and R. G. Korteling in Proceedings of the Eighth International Conference on High Energy Physics and Nuclear Structure (1979), Abstract 4A17 (unpublished) and private communication.

[28]R. E. L Green and R. G. Korteling, Nucl. Instrum. Methods **185**, 195 (1981).

[29]M. Fatyga, K. Kwiatkowski, H. J. Karwowski, L. W. Woo, and V. E. Viola, Phys. Rev. C **32**, 1496 (1985).